

Organic single-photon switch

Anton Zasedatelev^{1,*}, Anton V. Baranikov¹, Denis Sannikov¹, Darius Urbonas², Fabio Scafrimuto², Vladislav Yu. Shishkov^{1,3,4}, Evgeny S. Andrianov^{1,3,4}, Yurii E. Lozovik^{1,3,4,5}, Ullrich Scherf⁶, Thilo Stöferle², Rainer F. Mahrt², and Pavlos G. Lagoudakis^{1,7,*} ^a

¹*Skolkovo Institute of Science and Technology, Moscow, Russian Federation*

²*IBM Research Europe - Zurich, Säumerstrasse 4, Rüschlikon 8803, Switzerland*

³*Dukhov Research Institute of Automatics (VNIIA),*

22 Sushchevskaya, Moscow 127055, Russia

⁴*Moscow Institute of Physics and Technology,*

9 Institutskiy per., Dolgoprudny 141700, Moscow region, Russia

⁵*Institute for Spectroscopy RAS, 5 Fizicheskaya, Troitsk 142190, Russia*

⁶*Macromolecular Chemistry Group and Institute for Polymer Technology, Bergische Universität Wuppertal, Gauss-Strasse 20, 42119 Wuppertal, Germany and*

⁷*Department of Physics and Astronomy, University of Southampton,*

Southampton, SO17 1BJ, United Kingdom

(Dated: April 9, 2024)

^a Correspondence address:

Abstract

The recent progress in nanotechnology [1, 2] and single-molecule spectroscopy [3–5] paves the way for cost-effective organic quantum optical technologies emergent with a promise to real-life devices operating at ambient conditions. In this letter, we harness π -conjugated segments of an organic ladder-type polymer strongly coupled to a microcavity forming correlated collective dressed states of light, so-called of exciton-polariton condensates. We explore an efficient way for all-optical ultra-fast control over the macroscopic condensate wavefunction via a single photon. Obeying Bose statistics, exciton-polaritons exhibit an extreme nonlinearity undergoing bosonic stimulation [6] which we have managed to trigger at the single-photon level. Relying on the nature of organic matter to sustain stable excitons dressed with high energy molecular vibrations we have developed a principle that allows for single-photon nonlinearity operation at ambient conditions opening the door for practical implementations like sub-picosecond switching, amplification and all-optical logic at the fundamental limit of single light quanta.

Nonlinear optical phenomena are at heart of diverse applications today, facilitating telecommunication, data storage, high resolution microscopy, lithography etc. The implementation of nonlinear effects at single photon level is the holy grail in photonics that drives power consumption of all-optical switches, modulators and transistors towards their fundamental limit, and enables a number of unique applications of optical quantum control for new paradigms of computing, communication and metrology. Accordingly, considerable efforts have been invested toward the achievement of single-photon nonlinearity across a plethora of material systems and physical principles. Platforms range from ultracold atomic ensembles [7–9] to a single atom [10–13], including artificial, solid-state atoms [14–17] coupled to a high-finesse cavity have been developed addressing this problem. Until recently the nonlinear regime of cavity quantum electrodynamics (cQED) has been uniquely attributed to ultra-cold quantum emitters [18]. Recently, organics emerged as a new unique resource for quantum optics, making fascinating cQED phenomena easier to implement at much more relaxed experimental conditions [4, 5, 19]. In this respect, the regime of strong light-matter coupling of a single organic quantum emitter is of particular interest for ambient cQED. Recent progress in this field results in experimental realization of single molecule vacuum Rabi splitting [1, 20], Rabi oscillation and non-classical photon states generated in a strongly-coupled dye molecule at ambient conditions [19].

Nevertheless, single quantum emitters remain a fragile object to deal with, mainly because they require fine optical and mechanical controls as well as sophisticated photon detection techniques. Alternatively, the single-photon nonlinearity can be achieved by means of quantum interference in strongly correlated many-body systems, typically based on ultra-cold atomic ensembles [7–9]. Unlike their single emitter counterparts, such systems are more robust and scalable, but sophisticated cooling and states preparation techniques alongside high vacuum conditions compromise their use significantly. In contrast, organic molecular ensembles strongly coupled to a cavity combine the above concepts of cQED and correlated many-body physics giving rise for dressed light-matter states which surpass low temperature limitations [21]. The dressed states are also known as exciton-polaritons (from here on polaritons), in general. Obeying Bose statistics, under certain conditions polaritons undergo the transition to a macroscopically occupied state exhibiting off-diagonal long-range order - polariton condensate [22–24]. The correlated and highly nonlinear nature of polariton condensates [25] makes them outstanding candidates for integrated on-chip photonics [6, 26, 27].

Here, we demonstrate ultra-fast optical switching operational at the fundamental level of single quanta in ambient conditions, using a π -conjugated ladder-type polymer.

To investigate the potential of polariton condensates for ultra-low energy switching down to a single photon, we employ an organic semiconductor polymer microcavity consisting of a 35 nm thick film of π -conjugated polymer (MeLPPP) encapsulated in between 50 nm SiO_2 spacers which is sandwiched between SiO_2/Ta_2O_5 distributed Bragg reflectors (DBR) constituting a $\lambda/2$ optical cavity (see Methods). The structure design and related properties have been extensively studied in [6, 24]. Strong light-matter interaction gives rise to new composite states in the system: Frenkel polaritons which obey Bose-Einstein statistics at low density regime. To populate polariton states we first form an exciton reservoir by resonant optical pumping, as shown schematically in Fig.1a, that we direct on the sample at 45 deg incidence to minimise reflection losses. Excitons from the reservoir undergo multiple relaxation processes towards various final states including polaritons through the intracavity radiative pumping and vibron-assisted thermalization [28–30]. Recently, we have demonstrated the latter favours efficient exciton-to-polariton relaxation in organic systems exhibiting intense vibrational resonances and makes polariton condensation feasible at much lower excitation energy [6]. To exploit high-energy vibrons for exciton cooling we optimise the energy difference between exciton reservoir ($\hbar\omega_{exc}$) and the ground polariton state ($\hbar\omega_{pol}$), thus fulfil the following relaxation condition: $\hbar\omega_{exc} = \hbar\omega_{pol} + \hbar\omega_{vib}$, where $\hbar\omega_{vib} = 199 meV$ is the molecular vibron energy. By such optimized conditions we reach polariton condensation at low absorbed fluence $F_{th} \sim 8 \mu J/cm^2$ (corresponds to 300 pJ incident pump pulse energy). Above the threshold we observe superlinear increase of total output microcavity emission following stimulated cooling of excitons from the reservoir towards the ground polariton state as shown in Fig.1b.

The main idea behind extreme nonlinearity is illustrated in Fig.1a (bottom schematic): few polaritons injected by a seed pulse trigger the exciton avalanche cooling down to the ground polariton state via vibron-assisted bosonic stimulation and result in massively occupied degenerate state forming a polariton condensate. To test the bosonic stimulation principle at ultimately low switching energies of the seed beam we employ a recently developed technique of dynamic polariton condensation [6]. We use spectrally-filtered sub-picosecond long pulses tightly focused on the sample down to $5 \mu m$ spot within $\pm 0.2 \mu m^{-1}$ wavevector range seeding the ground polariton state resonantly as schematically depicted in Fig.1a

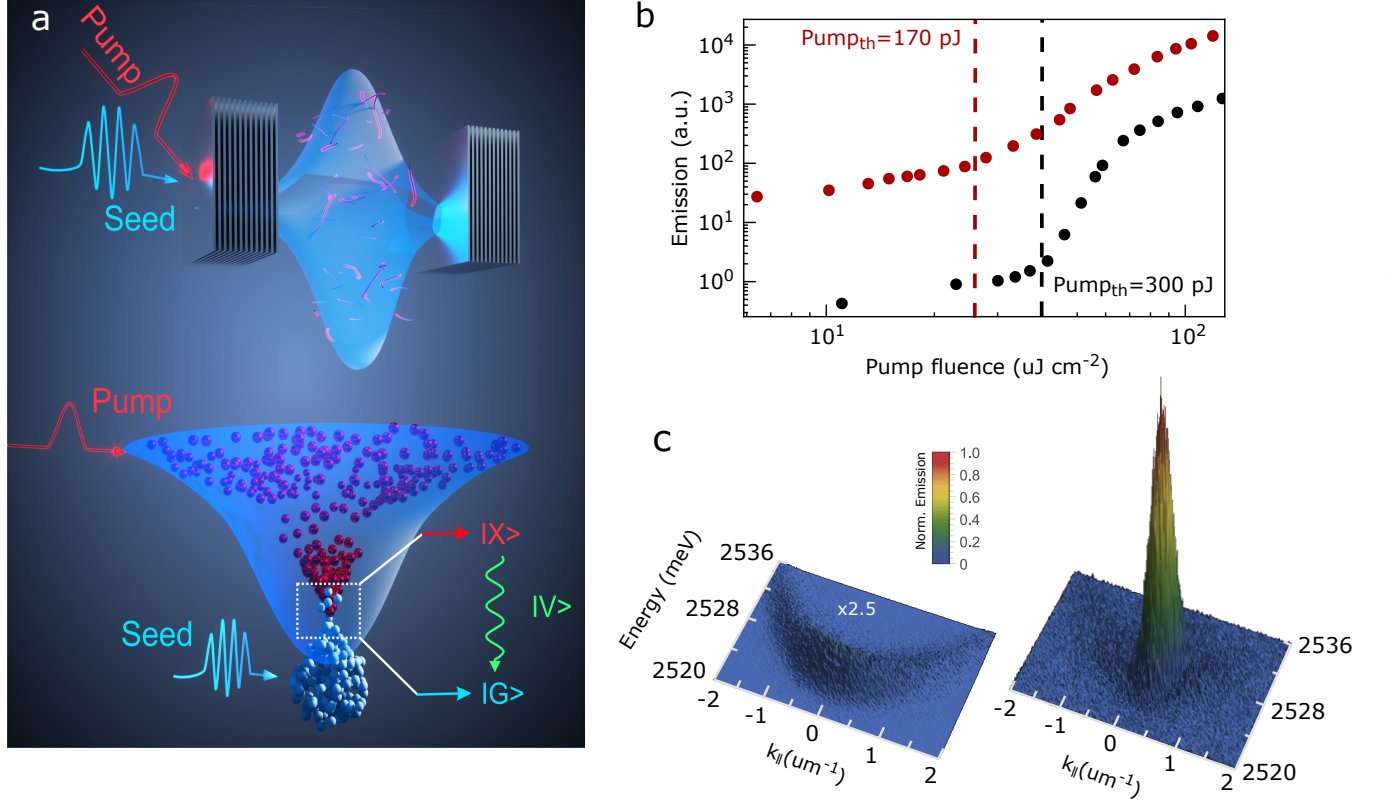


FIG. 1. **The principle of the extreme nonlinearity in organics.** **a**, Schematic illustrates the principle of stimulated exciton cooling towards the polariton ground state. **b**, Integrated emission as a function of pump fluence plotted for the spontaneously built (black dots) and seeded (red dots) polariton condensates formed at the pump energy threshold of 300 pJ and 170 pJ respectively; as shown by vertical dashed lines. **c**, Energy, momentum (E, k) distribution for spontaneously built (left) and seeded (right) polariton condensates respectively. Incident pump fluence is $80 \mu\text{J}/\text{cm}^2$ ($P \sim 2P_{th}$), energy of the seed beam is 460 aJ.

(see Methods). To maximise efficiency of stimulation towards the condensate we optimise spatial and temporal overlap between the seed and pump beams accordingly. Finally, we attenuate the seed down to the level of 460 aJ per pulse corresponding to ~ 1140 polaritons resonantly injected to the ground state directly. Such a prearrangement in population of the ground polariton state increases the exciton-to-polariton relaxation rate drastically allowing for polariton condensation at the twice lower exciton reservoir density and boosting the total state's occupancy. According to the pump fluence dependence represented in Fig.1b, resonant seeding results in ~ 50 times higher integrated emission compared to the sponta-

neously built condensate. The stimulation effect on energy-momentum (E,k) distributions of the condensate is shown in Fig.1c (see Methods).

Started out from the sub-femtojoule seed pulses we further investigate potential control over the condensate occupancy by harnessing progressively smaller seed energy: from 26 aJ down to 4 aJ and 1 aJ pulses as shown in Fig.2a-c respectively. With decreasing energy of the seed we observe substantial reduction of the ground state population, although even at the lowest seed energy of 1 aJ carrying only 2.5 photons per pulse on average we are still able to resolve an increase in the condensate population. Figure 2d shows emission spectra obtained from integrated E,k distributions over the momentum range of $\pm 0.2 \mu m^{-1}$, exhibiting a clear contrast in population of seeded and spontaneously formed condensates. Comparing the spectral area in Fig.2d we detect nearly 55% difference in the ground state population for the case of 1 aJ seed. To minimize fluctuations of the condensate occupation number caused by pump induced exciton reservoir density variations we excite the system close to the gain saturation regime at $2F_{th}$ and integrate the output signal over 5000 single condensate realizations on the detector (see Methods).

To quantify the condensate nonlinearity upon seeding photon states, we introduce the contrast as the figure of merit parameter which relies on the ratio of integrated population at the ground state between spontaneously formed (P_{spont}) and seeded polariton condensates (P_{seed}): $Contrast = \frac{P_{seed}}{P_{spont}} - 1$. Our systematic study of the seeded condensation reveals nearly a power-law dependence on the average seed photon states as follows from the experimental data represented in Fig.3. We experimentally observe condensate switching triggered by the seed pulse carrying ~ 1.5 photons on average with a probability larger than 0.95. Figure 3 shows that the lowest limit of 2σ error bars exceeds 0% contrast level of unseeded condensate. To explain the experimentally observed behaviour we have developed a microscopic theory of the seeded vibron-mediated polariton condensation (see Methods and Sections I in Supplementary Information (SI) for further details). Numerical simulations agree well with the observed contrast dependence, as one can see from the fit in Fig.3 (solid curve). In-depth analysis of mechanisms behind the nonlinearity is represented in Section II of SI. It is worth noting, the principle of switching allows for single photon operation as follows from the simulations. Our model predicts a contrast $\sim 20\%$ for single-photon seed.

However, despite the good agreement between experimental data and theory care has to be taken in approaching the single photon regime experimentally as the statistical proper-

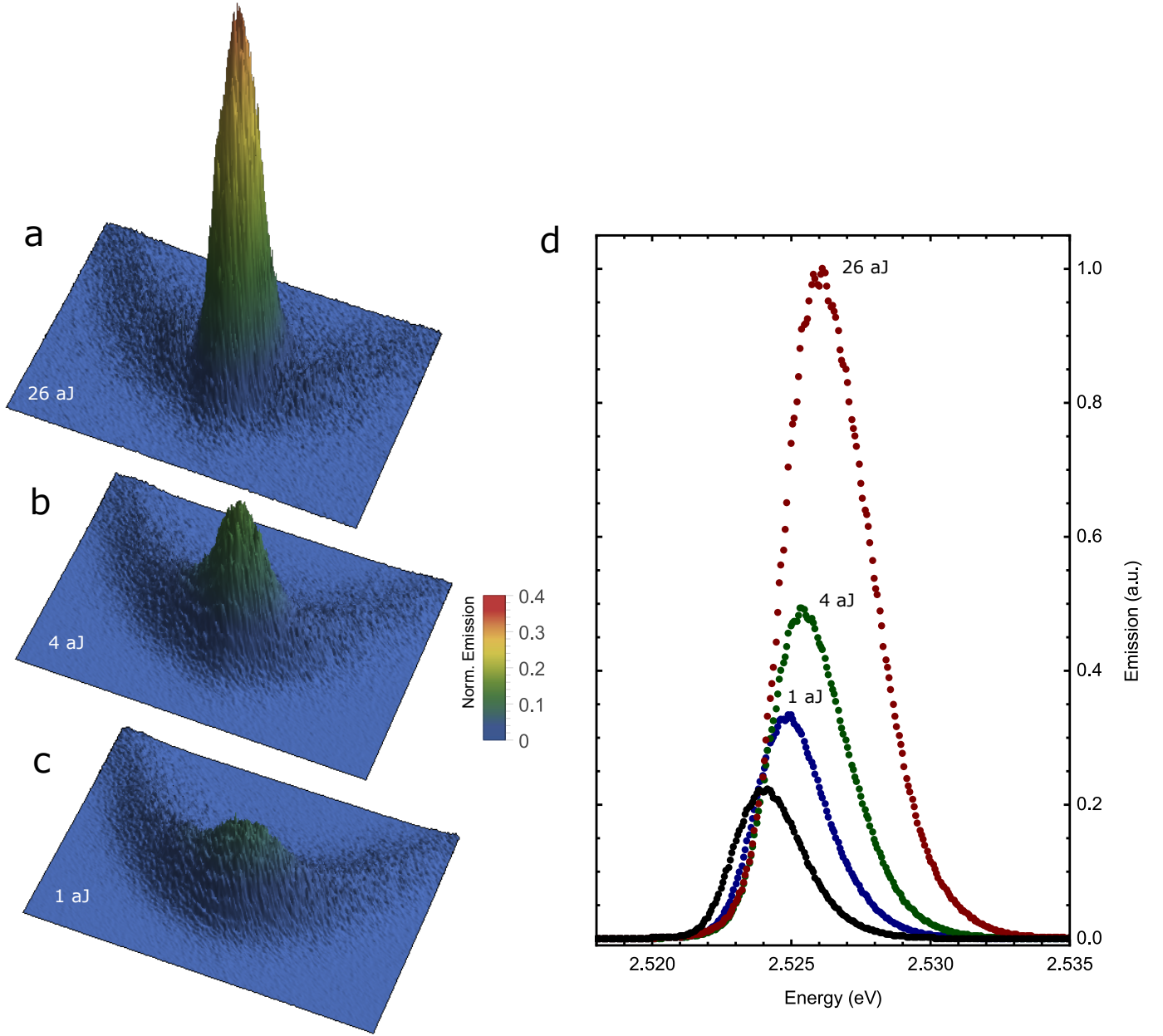


FIG. 2. **Atto-Joule polariton switch.** **a,b,c**, Energy, momentum (E, k) distributions of 5000 condensates realizations each seeded with 26 aJ, 4 aJ and 1 aJ pulses respectively. **d**, Emission spectra obtained from (E, k) distributions **a-c** by integrating over $\pm 0.2 \mu m^{-1}$ in momentum space. Red, green and blue dots correspond to the polariton condensate seeded with 26 aJ, 4 aJ and 1 aJ pulses respectively, while black dots display emission spectrum of the spontaneously built condensate.

ties of the source can no longer be neglected. The seed, being a laser-like source, obeys Poisson photon number distribution inherited from the laser generating the supercontinuum beam (see Methods). Therefore at the few-photon regime, the tail of the distribution containing higher photon number states might contribute to polariton stimulation significantly. Following Poisson statistics, the probability of having n photons in the distribution scales with its maximum at $\langle n \rangle$ average photons as $\frac{\langle n \rangle!}{n!} \langle n \rangle^{n-\langle n \rangle}$. In the case of a seed pulse with 4 photons on average, although the majority of realisations exhibits 4 photons per pulse, there are some relatively rare events containing significantly more photons per pulse. For instance 10-photon events are possible but with ~ 37 times lower probability. Since in the above experiments we integrate over thousands of single-condensate realizations our results might be affected by such higher photon number states, providing a stronger stimulation rate and being accumulated with a large weight in the total registered polariton population. In other words it is not clear now whether the few-photon control over the condensate is experimentally feasible by every seed pulse or cumulative effect is observed.

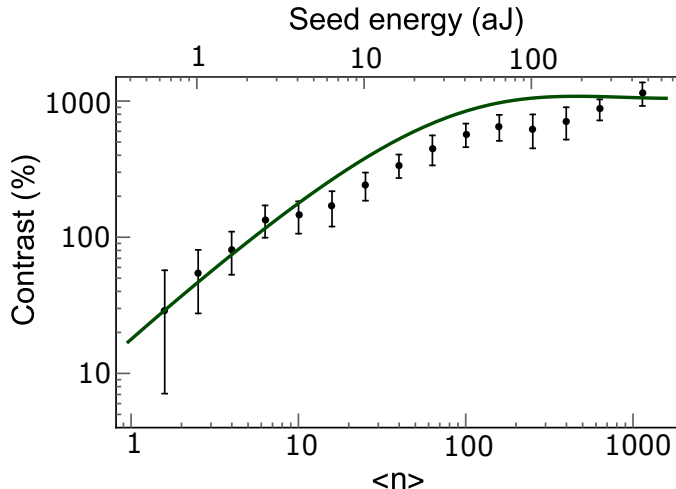


FIG. 3. **The switching contrast at the single-photon level.** The contrast in population between seeded and spontaneously built polariton condensates as the function of seed energy and average photon number per pulse. Solid curve shows the result of numerical simulations carried out according with the theoretical model.

We address this problem by implementing a single-shot measurement scheme allowing for pulse-to-pulse analysis of the condensate population (see Methods). We employ the same pumping and seeding excitation geometries but we detect condensate population in real space

using appropriate filtering in momentum space within $\pm 1\mu m^{-1}$ (see Methods). We perform these measurements by seeding the ground state for 300 sequential pulses then we switch the seed beam off allowing for 300 realizations of spontaneously built polariton condensates and repeat the whole sequence again as shown in Fig.4a-e. A clear contrast for single-condensate realisations with an average value of about 350%, 160%, 60%, 25% and 11% assessed for the seed containing $\langle n \rangle$ equals 600, 60, 9.3, 2.7, and 1 photon per pulse respectively can be seen. Statistical analysis of 900 realizations elucidates the effect of single-photon control over the total polariton population at the condensate induced by every seed pulse. Right panels of Fig.4a-e show histograms of the total polariton population at single spontaneously built (black) and seeded (red) condensate realizations fitted by Gaussian distributions. As the experimental distributions are close to Gaussian our statistical analysis yields almost the same mean contrast values of 360%, 160%, 63%, 26% and 11% as shown in Fig.4f. Moreover, the results of single condensate realisations are consistent with integrated measurements discussed above and are well supported by the theory.

In conclusion, we exemplify the outstanding single-photon nonlinearity discovered in organic polariton condensates. The general mechanism that enables nonlinearity at the quantum limit is the bosonic stimulation principle inherited for exciton-polaritons regardless of the material systems. Our report convincingly demonstrates few-photon control over the polariton occupancy of the condensate with unprecedented gain of ~ 23000 secondary polaritons per single resonantly injected seed polariton. We experimentally demonstrate for the first time at ambient conditions single-photon polariton condensate ultrafast switching with a contrast of $\sim 11\%$ following the pulse-to-pulse analysis of the single-condensate realisations and $\sim 20\%$ according to integrated measurements. Organic materials offer great potential for integration on a chip together with their identical chemical and optical characteristics which can be easily altered spanning a range from ultraviolet to the near infrared spectrum. Ultimately, it opens a new horizon for all-optical manipulation, data processing and detection at the single-photon level bridging quantum properties of light with classical phenomena of massively occupied states such as mixed light-matter Bose-Einstein condensates.

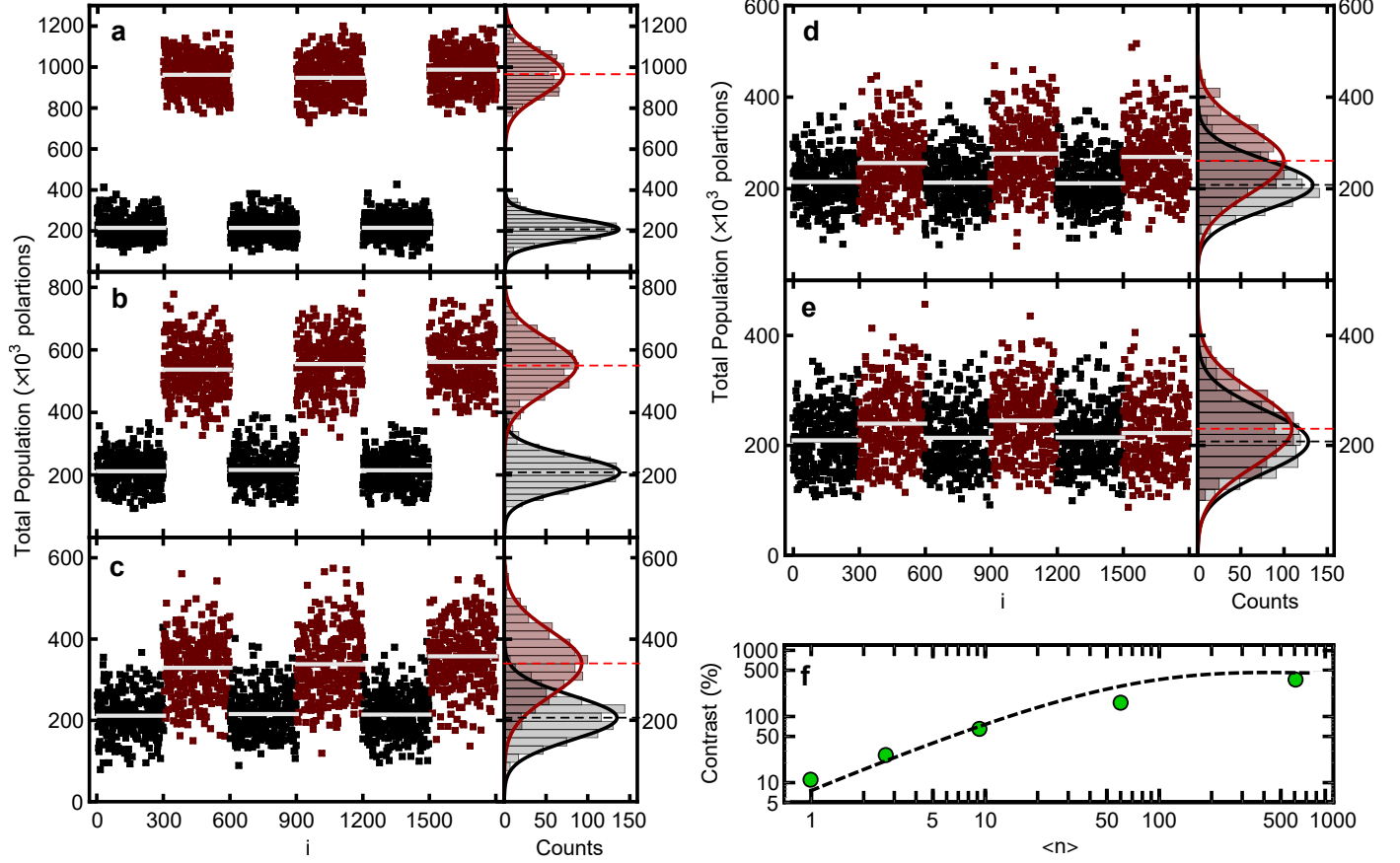


FIG. 4. **Single-photon switching at single-condensate realisations.** **a-e**, Total polariton populations recorded within $\pm 1\mu\text{m}^{-1}$ wavevector range in the single-shot regime for a sequence of 300-to-300 spontaneously built (black dots) and seeded (red dots) polariton condensate realisations. Seeded realisations are triggered by $\langle n \rangle$ equals 600, 60, 9.3, 2.7, and 1 photon per pulse on average as shown in **a-e** respectively. Right panels represent histograms of total polariton population within single-condensate realisations seeded with correspondent $\langle n \rangle$ photon number state (red) as well histograms of the spontaneously built condensate (black), both fitted by Gaussian distributions accordingly. **f**, Switching contrast versus average number of photons per seed pulse $\langle n \rangle$ acquired from statistical analysis according to the histograms.

-
- [1] Chikkaraddy, R. *et al.* Single-molecule strong coupling at room temperature in plasmonic nanocavities. *Nature* **535**, 128 (2016).
- [2] Hail, C.U. *et al.* Nanoprinting organic molecules at the quantum level. *Nat. Commun.* **10**, 1880 (2019).
- [3] Maser, A. *et al.* Few-photon coherent nonlinear optics with a single molecule. *Nat. Photon.* **10**, 450 (2016).
- [4] Wang, D. *et al.* Coherent Coupling of a Single Molecule to a Scanning Fabry-Perot Microcavity. *Phys. Rev. X* **7**, 021014 (2017).
- [5] Wang, D. *et al.* Turning a molecule into a coherent two-level quantum system. *Nat. Phys.* **15**, 483 (2019).
- [6] Zasedatelev, A.V. *et al.* A room-temperature organic polariton transistor. *Nat. Photon.* **13**, 378 (2019).
- [7] Peyronel, T. *et al.* Quantum nonlinear optics with single photons enabled by strongly interacting atoms. *Nature* **488**, 57 (2012).
- [8] Chen, W. *et al.* All-Optical Switch and Transistor Gated by One Stored Photon. *Science* **341**, 768 (2013).
- [9] Gorniaczyk, H. *et al.* Single-Photon Transistor Mediated by Interstate Rydberg Interactions. *Phys. Rev. Lett.* **113**, 053601 (2014).
- [10] Reiserer, A. *et al.* Nondestructive Detection of an Optical Photon. *Science* **342**, 1349 (2013).
- [11] Shomroni, I. *et al.* All-optical routing of single photons by a one-atom switch controlled by a single photon. *Science* **346**, 903 (2014).
- [12] Tiecke, T.G. *et al.* Nanophotonic quantum phase switch with a single atom. *Nature* **508**, 241 (2014).
- [13] Hacker, B. *et al.* A photon–photon quantum gate based on a single atom in an optical resonator. *Nature* **536**, 193 (2016).
- [14] Volz, T. *et al.* Ultrafast all-optical switching by single photons. *Nat. Photon.* **6**, 605 (2012).
- [15] Giesz, V. *et al.* Coherent manipulation of a solid-state artificial atom with few photons. *Nat. Commun.* **7**, 11986 (2016).
- [16] Sun, S. *et al.* A single-photon switch and transistor enabled by a solid-state quantum memory.

Science **361**, 57 (2018).

- [17] Dietrich, C.P. *et al.* GaAs integrated quantum photonics: Towards compact and multi-functional quantum photonic integrated circuits. *Laser Photonics Rev.* **10**, 870 (2016).
- [18] Chang, D.E. *et al.* Quantum nonlinear optics — photon by photon. *Nat. Photon.* **6**, 685 (2014).
- [19] Ojambati, O.S. *et al.* Quantum electrodynamics at room temperature coupling a single vibrating molecule with a plasmonic nanocavity. *Nat. Commun.* **10**, 1049 (2019).
- [20] Liu, R. *et al.* Strong Light-Matter Interactions in Single Open Plasmonic Nanocavities at the Quantum Optics Limit. *Phys. Rev. Lett.* **118**, 237401 (2017).
- [21] Sanvitto, D., Kéna-Cohen, S., The road towards polaritonic devices. *Nat. Mater.* **15**, 1061 (2016).
- [22] Deng, H., Haug, H., Yamamoto, Y. Exciton-polariton Bose-Einstein condensation. *Rev. Mod. Phys.* **82**, 1489 (2010).
- [23] Kasprzak, J. *et al.* Bose-Einstein condensation of exciton polaritons. *Nature* **443**, 409-414 (2006).
- [24] Plumhof, J. D., Stöferle, T. Mai, L., Scherf, U. & Mahrt, R. F. Room-temperature bose-einstein condensation of cavity exciton-polaritons in a polymer. *Nat. Mater.* **13**, 247-252 (2014).
- [25] Carusotto, I., Ciuti, C. Quantum fluids of light. *Rev. Mod. Phys.* **85**, 299 (2013).
- [26] Lerario, G. *et al.* Room-temperature superfluidity in a polariton condensate. *Nat. Phys.* **13**, 837-841 (2017).
- [27] Sun, Z., Snoke, D.W. Optical switching with organics. *Nat. Photon.* **13**, 370 (2019).
- [28] Tartakovskii, A.I. *et al.* Raman scattering in strongly coupled organic semiconductor microcavities. *Phys. Rev. B* **63**, 121302 (2001).
- [29] Coles, D. M. *et al.* Vibrationally assisted polariton-relaxation processes in strongly coupled organic-semiconductor microcavities. *Adv. Funct. Mater.* **21**, 3691–3696 (2011).
- [30] Grant, R.T. *et al.* Efficient Radiative Pumping of Polaritons in a Strongly Coupled Microcavity by a Fluorescent Molecular Dye. *Adv. Opt. Mater.* **4**, 1615 (2016).

METHODS

Sample fabrication.

The sample is composed of a bottom distributed Bragg reflector (DBR), a central cavity defect region with an effective thickness slightly larger than half the exciton wavelength, and a top DBR on a fused silica substrate. The DBRs consist of alternating $\text{SiO}_2/\text{Ta}_2\text{O}_5$ quarter-wavelength-thick layers produced by sputter deposition (9+0.5 pairs for the bottom DBR, 6+0.5 for the top DBR). The center of the cavity consists of a polymer layer sandwiched within 50-nm spacer layers of sputtered SiO_2 . The SiO_2 spacer is sputtered on the organic using a SiO_2 sputter target. Methyl-substituted ladder-type poly(p-phenylene) (MeLPPP; $M_n = 31500$, $M_w = 79000$) was synthesized as described elsewhere [31]. MeLPPP is dissolved in toluene and spin-coated on the bottom spacer layer. The film thickness of approximately 35 nm is measured with a profilometer (Veeco Dektak).

Spectroscopy. The pump beam with 150-200 fs pulse duration was generated by a tunable optical parametric amplifier (Coherent OPerA SOLO) which was pumped by 500 Hz high energy Ti:Sapphire regenerative amplifier (Coherent Libra-HE). The center wavelength was adjusted with respect to experiments at 2.72 eV having 30 meV full-width at half-maximum (FWHM). The pulses were focused at the sample to a 20 μm spot and hit the sample at 45° . Filtered broadband white-light-continuum (WLC) generated in a sapphire plate with photon energies in the range 2.45 - 2.6 eV was utilized as the seed beam having 150-250 fs pulse duration. The seed beam was focused on the sample at the normal incidence to 5 μm spot size with a micro-objective (10x Nikon, 0.3 NA) which allows to seed the ground polariton state within a wavevector range of $\pm 0.2\mu\text{m}^{-1}$. In all measurements, temporal and spatial overlapping between the control and the pump beams were optimized by maximizing the signal of the output nonlinear emission from the sample. Temporal overlapping was varied by using a motorized translation stage with retroreflector in the seed beam optical path.

Integrated energy-momentum E, k distributions were acquired in transmission geometry. Output emission of the sample was collected with a 10X Mitutoyo plan apo infinity corrected objective (NA = 0.28) and coupled to a 750 mm spectrometer (Princeton Instruments SP2750) equipped with an electron multiplying CCD camera (Princeton Instruments ProEM 1024BX3). The emission was spectrally and in-plane wavevector resolved using

a 1200 grooves/mm grating and a slit width of 50 μm at the entrance of the spectrometer. To obtain the incident excitation density of the pump pulse, the average pump power was measured using a calibrated Si photodetector (Thorlabs-Det10/M) and an oscilloscope (Keysight DSOX3054T) for data acquisition. Accuracy verification of the power measurements was carried out by using two independent power meters: 1 - Si photodiode power sensor (Thorlabs-S120VC) with a power meter console (Thorlabs-PM100D), 2 - thermal power sensor (Thorlabs-S302C) equipped with the power meter console (Thorlabs-PM100D). The energy of the seed beam was calibrated by using standard power meter measurements and additionally verified through a single photon counting technique using a photon counting module (SPC-160, Becker & Hickl GMBH) and a single-photon avalanche Si photodiode (IDQ 100), for details see Fig.S4 in Section III of SI. All the measurements for Fig.2 and 3 are carried out under the same incident pump fluence of $F_{\text{pump}} = 80\mu\text{Jcm}^{-2}$ ($P \sim 2P_{th}$) to minimize noise level originating from pump power fluctuations and high nonlinearity of the sample above the threshold. Pump fluence dependencies in Fig.1b as well as spectra in Fig.2d and the contrast dependence in Fig.3 are plotted for the ground polariton state integrated within $\pm 0.2\mu\text{m}^{-1}$.

Polariton single-condensate realizations were investigated by means of single-shot real space imaging technique using the same pump conditions ($P \sim 2P_{th}$) with individual pulse control. The images were recorded by means of the electron multiplying CCD camera applying 100x EM gain and operating in a single frame acquisition mode. To get rid of non-condensed polariton density we filtered out the output emission above $\pm 1\mu\text{m}^{-1}$ in Fourier space. The single-condensate realisations in Fig.4a-e were recorded by seeding the ground state for 300 sequential pulses followed by seed beam off measurements that allow for 300 realizations of spontaneously built polariton condensates. The whole sequence was repeated three times for each seed pulse energy. The incident seed energy was stabilised at the level of 2% standard deviation. To reduce the noise originated from pump fluctuation we recorded the energy of incident pulses for each condensate realisation using calibrated Si photodetector and an oscilloscope and then extracted only realisations within 2% of tolerance interval. Statistical analysis and calculation of the single-realisation contrast in Fig.4a-e were carried out through processing of all 900 spontaneously built and 900 seeded condensate realisations for each seed state.

Theoretical model.

The system is treated microscopically by considering a thin organic active layer (MeLPPP) placed in the cavity excited by an external wave that corresponds to the pump beam. The pump wave induces the dipole moment transition of organics creating Frenkel-type excitons. In turn, the excitons interacts with both vibrons and cavity modes. Hereby we consider the pump exciting organic layer resonantly to the exciton transition. The Hamiltonian of the whole system has the following form:

$$\hat{H} = \hat{H}_{\text{cav}} + \hat{H}_{\text{exc}} + \hat{H}_{\text{vib}} + \hat{H}_{\text{exc-cav}} + \hat{H}_{\text{exc-vib}} + \hat{H}_{\text{exc-pump}} + \hat{H}_{\text{cav-seed}} \quad (1)$$

where the terms correspond to uncoupled cavity modes, excitons, vibrons, interactions between excitons and cavity modes, excitons and vibrons as well as interaction between excitons and external pump wave and cavity modes with the external seed wave, listed as they appear in Eq. (1). For further details see Section I in SI. On the next step we make a transformation from treating the system in form of uncoupled excitons and cavity modes to their hybridized solutions: exciton-polaritons. We diagonalize the corresponding part of the full Hamiltonian, namely $\hat{H}_{\text{cav}} + \hat{H}_{\text{exc}} + \hat{H}_{\text{exc-cav}}$, and derive operators for lower polaritons $\hat{s}_{\text{low}\mathbf{k}}$ and upper polaritons $\hat{s}_{\text{up}\mathbf{k}}$ using the transformation below:

$$\hat{s}_{\text{up}\mathbf{k}} = \hat{c}_{\text{exc}\mathbf{k}} \cos \varphi_{\mathbf{k}} + \hat{a}_{\text{cav}\mathbf{k}} \sin \varphi_{\mathbf{k}} \quad (2)$$

$$\hat{s}_{\text{low}\mathbf{k}} = \hat{a}_{\text{cav}\mathbf{k}} \cos \varphi_{\mathbf{k}} - \hat{c}_{\text{exc}\mathbf{k}} \sin \varphi_{\mathbf{k}} \quad (3)$$

where $\hat{a}_{\text{cav}\mathbf{k}}$ and $\hat{c}_{\text{exc}\mathbf{k}}$ are cavity photon and exciton operators respectively, and

$$\varphi_{\mathbf{k}} = \frac{1}{2} \arctg \left(\frac{2\Omega_{\text{Rk}}}{\omega_{\text{exc}} - \omega_{\text{cav}\mathbf{k}}} \right) \quad (4)$$

Following the transformations above the full Hamiltonian (1) takes the form

$$\begin{aligned} \hat{H} = & \sum_{\mathbf{k}} \hbar \omega_{\text{up}\mathbf{k}} \hat{s}_{\text{up}\mathbf{k}}^\dagger \hat{s}_{\text{up}\mathbf{k}} + \sum_{\mathbf{k}} \hbar \omega_{\text{low}\mathbf{k}} \hat{s}_{\text{low}\mathbf{k}}^\dagger \hat{s}_{\text{low}\mathbf{k}} + \sum_{\mathbf{q}} \hbar \omega_{\text{vib}} \hat{b}_{\mathbf{q}}^\dagger \hat{b}_{\mathbf{q}} + \\ & + \sum_{\mathbf{k}} \sum_{\mathbf{k}'} \hbar g \left(\hat{s}_{\text{up}\mathbf{k}}^\dagger \cos \varphi_{\mathbf{k}} - \hat{s}_{\text{low}\mathbf{k}}^\dagger \sin \varphi_{\mathbf{k}} \right) \left(\hat{s}_{\text{up}\mathbf{k}'} \cos \varphi_{\mathbf{k}'} - \hat{s}_{\text{low}\mathbf{k}'} \sin \varphi_{\mathbf{k}'} \right) \left(\hat{b}_{-(\mathbf{k}-\mathbf{k}')}^\dagger + \hat{b}_{\mathbf{k}-\mathbf{k}'} \right) + \\ & + \sum_{\mathbf{k}} \hbar \Omega_{\mathbf{k}}(t) \left(\left(\hat{s}_{\text{up}\mathbf{k}}^\dagger \cos \varphi_{\mathbf{k}} - \hat{s}_{\text{low}\mathbf{k}}^\dagger \sin \varphi_{\mathbf{k}} \right) e^{-i\omega_{\Omega}t} + \left(\hat{s}_{\text{up}\mathbf{k}'} \cos \varphi_{\mathbf{k}'} - \hat{s}_{\text{low}\mathbf{k}'} \sin \varphi_{\mathbf{k}'} \right) e^{i\omega_{\Omega}t} \right) + \\ & + \sum_{\mathbf{k}} \hbar W_{\mathbf{k}}(t) \left(\left(\hat{s}_{\text{up}\mathbf{k}}^\dagger \cos \varphi_{\mathbf{k}} - \hat{s}_{\text{low}\mathbf{k}}^\dagger \sin \varphi_{\mathbf{k}} \right) e^{-i\omega_W t} + \left(\hat{s}_{\text{up}\mathbf{k}'} \cos \varphi_{\mathbf{k}'} - \hat{s}_{\text{low}\mathbf{k}'} \sin \varphi_{\mathbf{k}'} \right) e^{i\omega_W t} \right) \end{aligned} \quad (5)$$

The polaritons and vibrons interact with the environment that in turn initiates relaxation processes. We describe the relaxation processes within the formalism of Lindblad superoperators for a general density matrix $\hat{\rho}$ of both polaritons and vibrons. The Lindblad superoperators for the lower, upper polaritons and vibrons respectively have the form

$$L_{\text{low}}(\hat{\rho}) = \sum_{\mathbf{k}} \frac{\gamma_{\text{low}\mathbf{k}}}{2} \left(2\hat{s}_{\text{low}\mathbf{k}}\hat{\rho}\hat{s}_{\text{low}\mathbf{k}}^\dagger - \hat{s}_{\text{low}\mathbf{k}}^\dagger\hat{s}_{\text{low}\mathbf{k}}\hat{\rho} - \hat{\rho}\hat{s}_{\text{low}\mathbf{k}}^\dagger\hat{s}_{\text{low}\mathbf{k}} \right) \quad (6)$$

$$L_{\text{up}}(\hat{\rho}) = \sum_{\mathbf{k}} \frac{\gamma_{\text{up}\mathbf{k}}}{2} \left(2\hat{s}_{\text{up}\mathbf{k}}\hat{\rho}\hat{s}_{\text{up}\mathbf{k}}^\dagger - \hat{s}_{\text{up}\mathbf{k}}^\dagger\hat{s}_{\text{up}\mathbf{k}}\hat{\rho} - \hat{\rho}\hat{s}_{\text{up}\mathbf{k}}^\dagger\hat{s}_{\text{up}\mathbf{k}} \right) \quad (7)$$

$$L_{\text{vib}}(\hat{\rho}) = \sum_{\mathbf{q}} \frac{\gamma_{\text{vib}}}{2} (1 + n_{\text{vib}}^{\text{th}}) \left(2\hat{b}_{\mathbf{q}}\hat{\rho}\hat{b}_{\mathbf{q}}^\dagger - \hat{b}_{\mathbf{q}}^\dagger\hat{b}_{\mathbf{q}}\hat{\rho} - \hat{\rho}\hat{b}_{\mathbf{q}}^\dagger\hat{b}_{\mathbf{q}} \right) + \sum_{\mathbf{q}} \frac{\gamma_{\text{vib}}}{2} n_{\text{vib}}^{\text{th}} \left(2\hat{b}_{\mathbf{q}}^\dagger\hat{\rho}\hat{b}_{\mathbf{q}} - \hat{b}_{\mathbf{q}}\hat{b}_{\mathbf{q}}^\dagger\hat{\rho} - \hat{\rho}\hat{b}_{\mathbf{q}}\hat{b}_{\mathbf{q}}^\dagger \right) \quad (8)$$

where $\gamma_{\text{low}\mathbf{k}}$, $\gamma_{\text{up}\mathbf{k}}$ and γ_{vib} are the dissipation rates of lower, upper polaritons and the vibrons respectively, and $n_{\text{vib}}^{\text{th}} = 1/(\exp(\hbar\omega_{\text{vib}}/T) - 1)$ is the thermal distribution of vibrons at an effective MeLPPP temperature T .

Thermalization of the lower polaritons is described by the following Lindblad term:

$$\hat{L}_{\text{th}}(\hat{\rho}) = \sum_{\mathbf{k}_1, \mathbf{k}_2} \frac{\gamma_{\text{low}}^{\mathbf{k}_1\mathbf{k}_2}}{2} \left(2\hat{s}_{\text{low}\mathbf{k}_2}\hat{s}_{\text{low}\mathbf{k}_1}^\dagger\hat{\rho}\hat{s}_{\text{low}\mathbf{k}_1}\hat{s}_{\text{low}\mathbf{k}_2}^\dagger - \hat{s}_{\text{low}\mathbf{k}_1}\hat{s}_{\text{low}\mathbf{k}_2}^\dagger\hat{s}_{\text{low}\mathbf{k}_2}\hat{s}_{\text{low}\mathbf{k}_1}^\dagger\hat{\rho} - \hat{\rho}\hat{s}_{\text{low}\mathbf{k}_1}\hat{s}_{\text{low}\mathbf{k}_2}^\dagger\hat{s}_{\text{low}\mathbf{k}_2}\hat{s}_{\text{low}\mathbf{k}_1}^\dagger \right) \quad (9)$$

Here $\gamma_{\text{low}}^{\mathbf{k}_1\mathbf{k}_2}$ is the rate of energy flow from the lower polaritons having in-plane wavevector \mathbf{k}_2 towards ones with wavevector \mathbf{k}_1 . According to Kubo-Martin-Schwinger relation, the rate $\gamma_{\text{low}}^{\mathbf{k}_1\mathbf{k}_2}$ satisfies

$$\gamma_{\text{low}}^{\mathbf{k}_1\mathbf{k}_2} = \gamma_{\text{low}}^{\mathbf{k}_2\mathbf{k}_1} \exp\left(\frac{\omega_{\text{low}\mathbf{k}_2} - \omega_{\text{low}\mathbf{k}_1}}{T}\right) \quad (10)$$

where T is the effective lattice temperature.

Finally, we use a standard Lindblad master equations including the full Hamiltonian (5) and the Lindblad terms (6-9) described above:

$$\frac{d\hat{\rho}}{dt} = \frac{i}{\hbar} [\hat{\rho}, \hat{H}] + \hat{L}_{\text{up}}(\hat{\rho}) + \hat{L}_{\text{low}}(\hat{\rho}) + \hat{L}_{\text{vib}}(\hat{\rho}) + \hat{L}_{\text{th}}(\hat{\rho}) \quad (11)$$

For further details see Sections I and II in SI.

- [31] Scherf, U., Bohnen, A. & Müllen, K. Polyarylenes and poly (arylenevinylene) s, 9 The oxidized states of a (1, 4-phenylene) ladder polymer. *Makromol. Chem.* **193**, 1127–1133 (1992).

DATA AVAILABILITY

All data supporting this study are openly available from the University of Southampton repository at <https://doi.org/10.5258/SOTON/D1374>.

ACKNOWLEDGEMENTS

This work was supported by the Russian Scientific Foundation (RSF) grant No. 20-72-10145 and the UKs Engineering and Physical Sciences Research Council grant EP/M025330/1 to P.G.L on Hybrid Polaritonics. E.S.A. and V.Yu.Sh. thank the Foundation for the Advancement of Theoretical Physics and Mathematics Basis. Yu.E.L. acknowledges support by Program of Basic Research of the National Research University Higher School of Economics. D.U., F.S. and T.S. acknowledge support by QuantERA project RouTe (SNSF Grant No. 20QT21 175389). P.G.L, D.U., T.S. and R.F.M. acknowledge support by European H2020-FETOPEN project POLLOC (Grant No. 899141).

AUTHOR CONTRIBUTIONS

A.Z., A.V.B. and D.S. performed the experiments and analysed the data. D.U., F.S., T.S., and R.F.M. contributed to the design and fabrication of the organic microcavity. U.S. synthesised the organic material. V.Yu.Sh., E.S.A. and Yu.E.L. developed microscopic theory and carried out numerical simulations. A.Z. and P.G.L. designed and led the research. The manuscript was written through contributions from all authors. All authors have given approval to the final version of the manuscript.

ADDITIONAL INFORMATION

The authors declare no competing financial interests.

Supplementary Information: Organic single-photon switch

I. MICROSCOPIC THEORY OF VIBRON-MEDIATED POLARITON CONDENSATION

We consider a nonequilibrium microscopic model which describes an ensemble of organic molecules with vibrationally dressed electronic transitions and coupled to cavity modes carrying different in-plane momenta $\hbar\mathbf{k}_{\parallel}$ (hereinafter $\hbar\mathbf{k}$). The electronic transition being localised at molecules are effectively treated as Frenkel-type excitons, where each excitation can be described by the Pauli creation and annihilation operators acting on a single molecule. As the system excited in resonance with excitons (see Methods) we introduce an extra term coupling excitons with an external pump electromagnetic field. In addition, we implement the coupling term for a weak electromagnetic field resonantly seeding the ground polariton state of the system. Hereby, the full Hamiltonian of the systems reads:

$$\hat{H} = \hat{H}_{\text{cav}} + \hat{H}_{\text{exc}} + \hat{H}_{\text{vib}} + \hat{H}_{\text{exc-cav}} + \hat{H}_{\text{exc-vib}} + \hat{H}_{\text{exc-pump}} + \hat{H}_{\text{cav-seed}} \quad (1)$$

The Hamiltonian of the cavity \hat{H}_{cav} is

$$\hat{H}_{\text{cav}} = \sum_{\mathbf{k}} \hbar\omega_{\text{cav}\mathbf{k}} \hat{a}_{\text{cav}\mathbf{k}}^{\dagger} \hat{a}_{\text{cav}\mathbf{k}} \quad (2)$$

where $\hat{a}_{\text{cav}\mathbf{k}}^{\dagger}$ and $\hat{a}_{\text{cav}\mathbf{k}}$ are the creation and annihilation operators for a photon in the cavity which obey commutation relation $[\hat{a}_{\text{cav}\mathbf{k}}, \hat{a}_{\text{cav}\mathbf{k}'}^{\dagger}] = \delta_{\mathbf{k},\mathbf{k}'}$, the wavevector \mathbf{k} corresponds to in-plane momentum $\hbar\mathbf{k}$, and $\omega_{\text{cav}\mathbf{k}}$ is the eigenfrequency of the cavity mode with the in-plane wavevector \mathbf{k} .

The Hamiltonian of the excitons \hat{H}_{exc} is

$$\hat{H}_{\text{exc}} = \sum_j \hbar\omega_{\text{exc}} \hat{\sigma}_{\text{exc}j}^{\dagger} \hat{\sigma}_{\text{exc}j} \quad (3)$$

where ω_{exc} is the eigenfrequency of the excitons, $\hat{\sigma}_{\text{exc}j}^{\dagger}$ and $\hat{\sigma}_{\text{exc}j}$ are the creation and annihilation operators of the exciton of a single π -conjugated segment of MeLPPP located at the point \mathbf{r}_j . These operators obey commutation relation $\hat{\sigma}_{\text{exc}j} \hat{\sigma}_{\text{exc}j'}^{\dagger} + \hat{\sigma}_{\text{exc}j'}^{\dagger} \hat{\sigma}_{\text{exc}j} = \delta_{j,j'}$. Below we consider the case of small probability for the exciton to be found in an excited state. In this case the approximate commutation relation $[\hat{\sigma}_{\text{exc}j}, \hat{\sigma}_{\text{exc}j'}^{\dagger}] \approx \delta_{j,j'}$ is valid.

The Hamiltonian of interaction between excitons and cavity modes $\hat{H}_{\text{exc-cav}}$ is a multi-mode Jaynes-Cummings Hamiltonian [4]

$$\hat{H}_{\text{exc-cav}} = \sum_{\mathbf{k}, j} \hbar \Omega_{1\mathbf{R}\mathbf{k}} \left(\hat{\sigma}_{\text{exc}j}^{\dagger} \hat{a}_{\text{cav}\mathbf{k}} e^{i\mathbf{k}\mathbf{r}_j} + \hat{\sigma}_{\text{exc}j} \hat{a}_{\text{cav}\mathbf{k}}^{\dagger} e^{-i\mathbf{k}\mathbf{r}_j} \right) \quad (4)$$

where $\Omega_{1\mathbf{R}\mathbf{k}}$ is the Rabi frequency of interaction between an exciton placed at \mathbf{r}_j and a cavity mode with the in-plane wavevector \mathbf{k} . Here we suppose that electric field of the \mathbf{k} th mode is distributed in plane parallel to the mirrors according to $e^{i\mathbf{k}\mathbf{r}}$ and constant in the anti-node position where the MeLPPP layer is located. It is reasonable approximation since we deal with the microcavity carrying a single fundamental $\lambda/2$ mode and containing 35 nm thin MeLPPP layer at the center, which is much smaller than the wavelength λ . The explicit expression for the Rabi frequency $\Omega_{1\mathbf{R}\mathbf{k}}$ is $\Omega_{1\mathbf{R}\mathbf{k}} = -\mathbf{E}_{\mathbf{k}}\mathbf{d}/\hbar$, where \mathbf{d} is the transition dipole momentum of the exciton and $E_{\mathbf{k}}$ is the electric field amplitude per "one photon" in the cavity with the in-plane momentum $\hbar\mathbf{k}$.

It is convenient to introduce the collective operator effectively describing all excitons, namely,

$$\hat{c}_{\text{exc}\mathbf{k}} = \frac{1}{\sqrt{N_{\text{mol}}}} \sum_j \hat{\sigma}_{\text{exc}j} e^{i\mathbf{k}\mathbf{r}_j} \quad (5)$$

where N_{mol} is the total number of MeLPPP π -conjugated segments and \mathbf{k} is the wavevector. Operators $\hat{c}_{\text{exc}\mathbf{k}}^{\dagger}$ and $\hat{c}_{\text{exc}\mathbf{k}}$ are the creation and annihilation operators of the excitons which obey commutation relation $[\hat{c}_{\text{exc}\mathbf{k}}, \hat{c}_{\text{exc}\mathbf{k}'}^{\dagger}] = \delta_{\mathbf{k}, \mathbf{k}'}$. Using the operators $\hat{c}_{\text{exc}\mathbf{k}}$ we rewrite the Hamiltonians (3) and (4) in the following form

$$\hat{H}_{\text{exc}} = \sum_{\mathbf{k}} \hbar \omega_{\text{exc}} \hat{c}_{\text{exc}\mathbf{k}}^{\dagger} \hat{c}_{\text{exc}\mathbf{k}} \quad (6)$$

where $\omega_{\text{exc}\mathbf{k}}$ is the eigenfrequency of the exciton with the wavevector \mathbf{k} .

$$\hat{H}_{\text{exc-cav}} = \sum_{\mathbf{k}} \hbar \Omega_{\mathbf{R}\mathbf{k}} \left(\hat{c}_{\text{exc}\mathbf{k}}^{\dagger} \hat{a}_{\text{cav}\mathbf{k}} + \hat{c}_{\text{exc}\mathbf{k}} \hat{a}_{\text{cav}\mathbf{k}}^{\dagger} \right) \quad (7)$$

where $\Omega_{\mathbf{R}\mathbf{k}} = \sqrt{N_{\text{mol}}} \Omega_{1\mathbf{R}\mathbf{k}}$ is the Rabi frequency of exciton-photon interaction for the excitons and the cavity mode with $\hbar\mathbf{k}$ in-plane momentum.

The Hamiltonian of vibrons \hat{H}_{vib} is

$$\hat{H}_{\text{vib}} = \sum_j \hbar \omega_{\text{vib}} \hat{b}_j^{\dagger} \hat{b}_j \quad (8)$$

where \hat{b}_j^\dagger and \hat{b}_j are the creation and annihilation operators of vibrons which obey commutation relation $[\hat{b}_j, \hat{b}_{j'}^\dagger] = \delta_{j,j'}$.

The Hamiltonian of the interaction between the excitons and vibrons at a single elemental cite of MeLPPP is Fröhlich-type Hamiltonian [2]

$$\hat{H}_{\text{exc-vib}} = \sum_j \hbar g \hat{\sigma}_j^\dagger \hat{\sigma}_j (\hat{b}_j + b_j^\dagger) \quad (9)$$

where the g is the interaction constant between the excitons and vibrons.

Following the same momentum space representation, it is convenient to introduce collective vibron operators according to

$$\hat{b}_{\mathbf{q}} = \frac{1}{\sqrt{N_{\text{mol}}}} \sum_j \hat{b}_j e^{i\mathbf{q}\mathbf{r}_j} \quad (10)$$

Under the transformation (5) and (10) the Hamiltonian of collective vibrons $\hat{b}_{\mathbf{k}}$ and its interaction with collective excitons $\hat{c}_{\text{exc}\mathbf{k}}$ takes the form

$$\hat{H}_{\text{vib}} = \sum_{\mathbf{q}} \hbar \omega_{\text{vib}} \hat{b}_{\mathbf{q}}^\dagger \hat{b}_{\mathbf{q}} \quad (11)$$

$$\hat{H}_{\text{exc-vib}} = \sum_{\mathbf{k}} \sum_{\mathbf{k}'} \hbar g \hat{c}_{\text{exc}\mathbf{k}}^\dagger \hat{c}_{\text{exc}\mathbf{k}'} (\hat{b}_{-(\mathbf{k}-\mathbf{k}')}^\dagger + \hat{b}_{\mathbf{k}-\mathbf{k}'}) \quad (12)$$

where $\hat{b}_{\mathbf{q}}^\dagger$ and $\hat{b}_{\mathbf{q}}$ are the creation and annihilation operators of the vibrons which obey commutation relation $[\hat{b}_{\mathbf{q}}, \hat{b}_{\mathbf{q}'}^\dagger] = \delta_{\mathbf{q},\mathbf{q}'}$, the vector \mathbf{q} is in-plane wavevector of the vibrons, ω_{vib} is the eigenfrequency of the vibrons with the in-plane wavevector \mathbf{q} . Note that momenta of excitons and vibrons in Eq. (12) fulfils momentum conservation law.

The Hamiltonian of the interaction between excitons and cavity modes $\hat{H}_{\text{exc-cav}}$ is

$$\hat{H}_{\text{exc-cav}} = \sum_{\mathbf{k}} \hbar \Omega_{\mathbf{R}\mathbf{k}} (\hat{c}_{\text{exc}\mathbf{k}}^\dagger \hat{a}_{\text{cav}\mathbf{k}} + \hat{c}_{\text{exc}\mathbf{k}} \hat{a}_{\text{cav}\mathbf{k}}^\dagger) \quad (13)$$

where $\Omega_{\mathbf{R}\mathbf{k}}$ is the Rabi frequency of all excitons interacting with the cavity mode specified at the given in-plane momentum $\hbar\mathbf{k}$.

The Hamiltonian of the interaction between the excitons and the external pump field $\hat{H}_{\text{exc-pump}}$ is

$$\hat{H}_{\text{exc-pump}} = \sum_{\mathbf{k}} \hbar \Omega_{\mathbf{k}}(t) (\hat{c}_{\text{exc}\mathbf{k}}^\dagger e^{-i\omega_{\Omega}t} + \hat{c}_{\text{exc}\mathbf{k}} e^{i\omega_{\Omega}t}) \quad (14)$$

where $\Omega_{\mathbf{k}}(t)$ is proportional to the amplitude of the external field and ω_{Ω} is the frequency of the external field.

The term in Hamiltonian describing interaction between the seed electromagnetic field with cavity modes $\hat{H}_{\text{cav-seed}}$ is

$$\hat{H}_{\text{cav-seed}} = \sum_{\mathbf{k}} \hbar W_{\mathbf{k}}(t) \left(\hat{a}_{\text{cav}\mathbf{k}}^{\dagger} e^{-i\omega_W t} + \hat{a}_{\text{cav}\mathbf{k}} e^{i\omega_W t} \right) \quad (15)$$

where $W_{\mathbf{k}}(t)$ is proportional to the amplitude of the seed field and ω_W its frequency.

Next we diagonalize the light-matter interaction part of the Hamiltonian [4], namely $\hat{H}_{\text{cav}} + \hat{H}_{\text{exc}} + \hat{H}_{\text{exc-cav}}$. In the new basis of exciton-polariton states, annihilation operators for the lower $\hat{s}_{\text{low}\mathbf{k}}$ and upper $\hat{s}_{\text{up}\mathbf{k}}$ polaritons can be expressed through the standard transformation relations:

$$\hat{s}_{\text{low}\mathbf{k}} = \hat{a}_{\text{cav}\mathbf{k}} \cos \varphi_{\mathbf{k}} - \hat{c}_{\text{exc}\mathbf{k}} \sin \varphi_{\mathbf{k}} \quad (16)$$

$$\hat{s}_{\text{up}\mathbf{k}} = \hat{c}_{\text{exc}\mathbf{k}} \cos \varphi_{\mathbf{k}} + \hat{a}_{\text{cav}\mathbf{k}} \sin \varphi_{\mathbf{k}} \quad (17)$$

where

$$\varphi_{\mathbf{k}} = \frac{1}{2} \arctg \left(\frac{2\Omega_{\text{Rk}}}{\omega_{\text{exc}} - \omega_{\text{cav}\mathbf{k}}} \right) \quad (18)$$

Following the transformations above the full Hamiltonian (1) takes the form:

$$\begin{aligned} \hat{H} = & \sum_{\mathbf{k}} \hbar \omega_{\text{up}\mathbf{k}} \hat{s}_{\text{up}\mathbf{k}}^{\dagger} \hat{s}_{\text{up}\mathbf{k}} + \sum_{\mathbf{k}} \hbar \omega_{\text{low}\mathbf{k}} \hat{s}_{\text{low}\mathbf{k}}^{\dagger} \hat{s}_{\text{low}\mathbf{k}} + \sum_{\mathbf{q}} \hbar \omega_{\text{vib}} \hat{b}_{\mathbf{q}}^{\dagger} \hat{b}_{\mathbf{q}} + \\ & + \sum_{\mathbf{k}} \sum_{\mathbf{k}'} \hbar g \left(\hat{s}_{\text{up}\mathbf{k}}^{\dagger} \cos \varphi_{\mathbf{k}} - \hat{s}_{\text{low}\mathbf{k}}^{\dagger} \sin \varphi_{\mathbf{k}} \right) \left(\hat{s}_{\text{up}\mathbf{k}'} \cos \varphi_{\mathbf{k}'} - \hat{s}_{\text{low}\mathbf{k}'} \sin \varphi_{\mathbf{k}'} \right) \left(\hat{b}_{-(\mathbf{k}-\mathbf{k}')}^{\dagger} + \hat{b}_{\mathbf{k}-\mathbf{k}'} \right) + \\ & + \sum_{\mathbf{k}} \hbar \Omega_{\mathbf{k}}(t) \left(\left(\hat{s}_{\text{up}\mathbf{k}}^{\dagger} \cos \varphi_{\mathbf{k}} - \hat{s}_{\text{low}\mathbf{k}}^{\dagger} \sin \varphi_{\mathbf{k}} \right) e^{-i\omega_{\Omega} t} + \left(\hat{s}_{\text{up}\mathbf{k}'} \cos \varphi_{\mathbf{k}'} - \hat{s}_{\text{low}\mathbf{k}'} \sin \varphi_{\mathbf{k}'} \right) e^{i\omega_{\Omega} t} \right) + \\ & + \sum_{\mathbf{k}} \hbar W_{\mathbf{k}}(t) \left(\left(\hat{s}_{\text{up}\mathbf{k}}^{\dagger} \cos \varphi_{\mathbf{k}} - \hat{s}_{\text{low}\mathbf{k}}^{\dagger} \sin \varphi_{\mathbf{k}} \right) e^{-i\omega_W t} + \left(\hat{s}_{\text{up}\mathbf{k}'} \cos \varphi_{\mathbf{k}'} - \hat{s}_{\text{low}\mathbf{k}'} \sin \varphi_{\mathbf{k}'} \right) e^{i\omega_W t} \right) \end{aligned} \quad (19)$$

where the new eigenfrequencies are:

$$\omega_{\text{low}\mathbf{k}} = (\omega_{\text{exc}} + \omega_{\text{cav}\mathbf{k}})/2 - \sqrt{(\omega_{\text{exc}} - \omega_{\text{cav}\mathbf{k}})^2/4 + \Omega_{\text{Rk}}^2} \quad (20)$$

$$\omega_{\text{up}\mathbf{k}} = (\omega_{\text{exc}} + \omega_{\text{cav}\mathbf{k}})/2 + \sqrt{(\omega_{\text{exc}} - \omega_{\text{cav}\mathbf{k}})^2/4 + \Omega_{\text{Rk}}^2} \quad (21)$$

In turn, lower and upper polaritons as well as vibrons interact with the environment that inevitably leads to the relaxation processes. We consider the relaxation processes by means of Lindblad superoperators [3, 4] acting on the general density matrix operator $\hat{\rho}$

which ultimately describes the entire system including all the polaritons and vibrons. The Lindblad superoperators for the lower, upper polaritons and vibrons are read explicitly

$$L_{\text{low}}(\hat{\rho}) = \sum_{\mathbf{k}} \frac{\gamma_{\text{low}\mathbf{k}}}{2} \left(2\hat{s}_{\text{low}\mathbf{k}}\hat{\rho}\hat{s}_{\text{low}\mathbf{k}}^\dagger - \hat{s}_{\text{low}\mathbf{k}}^\dagger\hat{s}_{\text{low}\mathbf{k}}\hat{\rho} - \hat{\rho}\hat{s}_{\text{low}\mathbf{k}}^\dagger\hat{s}_{\text{low}\mathbf{k}} \right) \quad (22)$$

$$L_{\text{up}}(\hat{\rho}) = \sum_{\mathbf{k}} \frac{\gamma_{\text{up}\mathbf{k}}}{2} \left(2\hat{s}_{\text{up}\mathbf{k}}\hat{\rho}\hat{s}_{\text{up}\mathbf{k}}^\dagger - \hat{s}_{\text{up}\mathbf{k}}^\dagger\hat{s}_{\text{up}\mathbf{k}}\hat{\rho} - \hat{\rho}\hat{s}_{\text{up}\mathbf{k}}^\dagger\hat{s}_{\text{up}\mathbf{k}} \right) \quad (23)$$

$$L_{\text{vib}}(\hat{\rho}) = \sum_{\mathbf{q}} \frac{\gamma_{\text{vib}}}{2} (1 + n_{\text{vib}}^{\text{th}}) \left(2\hat{b}_{\mathbf{q}}\hat{\rho}\hat{b}_{\mathbf{q}}^\dagger - \hat{b}_{\mathbf{q}}^\dagger\hat{b}_{\mathbf{q}}\hat{\rho} - \hat{\rho}\hat{b}_{\mathbf{q}}^\dagger\hat{b}_{\mathbf{q}} \right) + \sum_{\mathbf{q}} \frac{\gamma_{\text{vib}}}{2} n_{\text{vib}}^{\text{th}} \left(2\hat{b}_{\mathbf{q}}^\dagger\hat{\rho}\hat{b}_{\mathbf{q}} - \hat{b}_{\mathbf{q}}\hat{b}_{\mathbf{q}}^\dagger\hat{\rho} - \hat{\rho}\hat{b}_{\mathbf{q}}\hat{b}_{\mathbf{q}}^\dagger \right) \quad (24)$$

where $\gamma_{\text{low}\mathbf{k}}$, $\gamma_{\text{up}\mathbf{k}}$ and γ_{vib} are the dissipation rates of lower, upper polaritons and the vibrons respectively, and $n_{\text{vib}}^{\text{th}} = 1/(\exp(\hbar\omega_{\text{vib}}/T) - 1)$ is the thermal distribution of vibrons at an effective lattice temperature T .

Thermalization of the lower polaritons is described by the following Lindblad superoperator:

$$\hat{L}_{\text{th}}(\hat{\rho}) = \sum_{\mathbf{k}_1, \mathbf{k}_2} \frac{\gamma_{\text{low}}^{\mathbf{k}_1\mathbf{k}_2}}{2} \left(2\hat{s}_{\text{low}\mathbf{k}_2}\hat{s}_{\text{low}\mathbf{k}_1}^\dagger\hat{\rho}\hat{s}_{\text{low}\mathbf{k}_1}\hat{s}_{\text{low}\mathbf{k}_2}^\dagger - \hat{s}_{\text{low}\mathbf{k}_1}\hat{s}_{\text{low}\mathbf{k}_2}^\dagger\hat{s}_{\text{low}\mathbf{k}_2}\hat{s}_{\text{low}\mathbf{k}_1}^\dagger\hat{\rho} - \hat{\rho}\hat{s}_{\text{low}\mathbf{k}_1}\hat{s}_{\text{low}\mathbf{k}_2}^\dagger\hat{s}_{\text{low}\mathbf{k}_2}\hat{s}_{\text{low}\mathbf{k}_1}^\dagger \right) \quad (25)$$

here $\gamma_{\text{low}}^{\mathbf{k}_1\mathbf{k}_2}$ is the rate of energy flow from the lower polaritons having in-plane wavevector \mathbf{k}_2 towards ones with wavevector \mathbf{k}_1 . According to Kubo-Martin-Schwinger relation, the rate $\gamma_{\text{low}}^{\mathbf{k}_1\mathbf{k}_2}$ is defined as

$$\gamma_{\text{low}}^{\mathbf{k}_1\mathbf{k}_2} = \gamma_{\text{low}}^{\mathbf{k}_2\mathbf{k}_1} \exp\left(\frac{\omega_{\text{low}\mathbf{k}_2} - \omega_{\text{low}\mathbf{k}_1}}{T}\right) \quad (26)$$

where T is the effective MeLPPP temperature.

The resulting master equation is

$$\frac{d\hat{\rho}}{dt} = \frac{i}{\hbar} [\hat{\rho}, \hat{H}] + \hat{L}_{\text{up}}(\hat{\rho}) + \hat{L}_{\text{low}}(\hat{\rho}) + \hat{L}_{\text{vib}}(\hat{\rho}) + \hat{L}_{\text{th}}(\hat{\rho}) \quad (27)$$

Further on we develop a mean-field theory [3] for the system described above. The mean-field theory describes dynamics of the system through evolution of amplitudes of upper polaritons, $s_{\text{up}\mathbf{k}} = \langle \hat{s}_{\text{up}\mathbf{k}} \rangle$, lower polaritons, $s_{\text{low}\mathbf{k}} = \langle \hat{s}_{\text{low}\mathbf{k}} \rangle$, and vibrons, $b_{\mathbf{q}} = \langle \hat{b}_{\mathbf{q}} \rangle$. To

derive these equations we use the following definition $\langle \dot{\hat{A}} \rangle = \text{Tr}(\dot{\hat{\rho}} \hat{A})$ and the master equation (27). The resulting mean-field equations take form

$$\frac{ds_{\text{up}\mathbf{k}}}{dt} = -i\omega_{\text{up}\mathbf{k}}s_{\text{up}\mathbf{k}} - \frac{1}{2}\gamma_{\text{up}\mathbf{k}}s_{\text{up}\mathbf{k}} + i \sum_{\mathbf{k}'} g \cos \varphi_{\mathbf{k}} \sin \varphi_{\mathbf{k}'} s_{\text{low}\mathbf{k}'} b_{\mathbf{k}-\mathbf{k}'} - i\Omega_{\mathbf{k}}(t) \cos \varphi_{\mathbf{k}} e^{-i\omega_{\Omega}t} \quad (28)$$

$$\begin{aligned} \frac{ds_{\text{low}\mathbf{k}}}{dt} = & -i\omega_{\text{low}\mathbf{k}}s_{\text{low}\mathbf{k}} - \frac{1}{2}\gamma_{\text{low}\mathbf{k}}s_{\text{low}\mathbf{k}} + i \sum_{\mathbf{k}'} g \cos \varphi_{\mathbf{k}'} \sin \varphi_{\mathbf{k}} s_{\text{up}\mathbf{k}'} b_{\mathbf{k}'-\mathbf{k}} + \\ & + i \sum_{\mathbf{k}'} g \sin \varphi_{\mathbf{k}'} \sin \varphi_{\mathbf{k}} s_{\text{low}\mathbf{k}'} (b_{\mathbf{k}'-\mathbf{k}}^* + b_{\mathbf{k}-\mathbf{k}'}) - i\Omega_{\mathbf{k}}(t) \sin \varphi_{\mathbf{k}} e^{-i\omega_{\Omega}t} - iW_{\mathbf{k}}(t) \cos \varphi_{\mathbf{k}} e^{-i\omega_W t} + \\ & + \frac{1}{2} \sum_{\mathbf{k}'} \left(\gamma_{\text{low}}^{\mathbf{k}\mathbf{k}'} |s_{\text{low}\mathbf{k}'}|^2 - \gamma_{\text{low}}^{\mathbf{k}'\mathbf{k}} (1 + |s_{\text{low}\mathbf{k}'}|^2) \right) s_{\text{low}\mathbf{k}} \quad (29) \end{aligned}$$

$$\begin{aligned} \frac{db_{\mathbf{q}}}{dt} = & -i\omega_{\text{vib}}b_{\mathbf{q}} - \frac{1}{2}\gamma_{\text{vib}}b_{\mathbf{q}} + i \sum_{\mathbf{k}'} g \cos \varphi_{\mathbf{k}'} \sin \varphi_{\mathbf{k}'-\mathbf{q}} s_{\text{up}\mathbf{k}'} s_{\text{low}\mathbf{k}'-\mathbf{q}}^* + \\ & + i \sum_{\mathbf{k}'} g \sin \varphi_{\mathbf{k}'} \sin \varphi_{\mathbf{k}'-\mathbf{q}} s_{\text{low}\mathbf{k}'} s_{\text{low}\mathbf{k}'-\mathbf{q}}^* \quad (30) \end{aligned}$$

Here we neglect non-resonant terms, that reasonably simplifies Eqs. (28)-(30).

To discretize the system we map its momenta states onto the energy space, moving from the continuum of wave vectors to a discrete set of frequencies. Note that since Eq. (29) contains spontaneous term, $1 + |s_{\text{low}\mathbf{k}'}|^2$, one should take into account the density of states. We consider a discrete finite set of frequencies $(\omega_0, \omega_1, \omega_2, \dots, \omega_N)$ with a sampling rate equal to $\delta\omega$, that is $\omega_{j+1} - \omega_j = \delta\omega$, where N means the total number of sampled frequencies. For the sake of simplicity we introduce the ground state frequency as $\omega_0 = \omega_{\text{low}(\mathbf{k}=0)}$ and determine the amplitude of the descretized lower polariton $s_{\text{low}\omega_j}$ with the eigenfrequency ω_j as follows

$$s_{\text{low}\omega_j} = \sum_{\mathbf{k}, \omega_j < \omega_{\text{low}\mathbf{k}} < \omega_j + \delta\omega} s_{\text{low}\mathbf{k}} \quad (31)$$

To calculate the number of states within the frequency range $\omega_j \leq \omega \leq \omega_j + \delta\omega$ we approximate lower polariton dispersion with a quadratic dependence $\omega_{\text{low}\mathbf{k}} = \omega_{\text{low}(\mathbf{k}=0)} + \alpha_{\text{cav}}\mathbf{k}^2$ so that it appears explicitly in the following form:

$$D_{\omega_j} = \sum_{\mathbf{k}, \omega_j < \omega_{\text{low}\mathbf{k}} < \omega_j + \delta\omega} 1 \approx \left(L n_{\text{MeLPPP}}^{1/3} \right) \frac{S}{(2\pi)^2} \int_{\omega_j < \omega_{\text{low}\mathbf{k}} < \omega_j + \delta\omega} d^2\mathbf{k} = \frac{S}{(2\pi)^2} \left(L n_{\text{MeLPPP}}^{1/3} \right) \frac{\pi}{\alpha} \delta\omega \quad (32)$$

where S is the area illuminated by the pump, L is the thickness of MeLPPP layer, n_{MeLPPP} is the concentration of MeLPPP. Unity in Eq. (32) denotes the one state with fixed wavevector \mathbf{k} . Note that the expression for D_{ω_j} is frequency independent in the case under consideration. If we substitute characteristic values of $S = 300 \mu\text{m}^2$, $L = 0.035 \mu\text{m}$, $n_{\text{MeLPPP}} \approx 10^6 \mu\text{m}^{-3}$ and $\alpha_{\text{cav}} = 2.2 \cdot 10^{-3} \text{ eV} \cdot \mu\text{m}^2$, then we obtain $D_{\omega_j} \approx 10^4 \cdot \delta\omega$ where $\delta\omega$ is measured in eV. The occupancy of the discrete modes at the lower polariton branch $n_{\text{low}j}$ takes the form

$$n_{\text{low}\omega_j} = \sum_{\mathbf{k}, \omega_j < \omega_{\text{low}\mathbf{k}} < \omega_j + \delta\omega} |s_{\text{low}\mathbf{k}}|^2 = \frac{|s_{\text{low}\omega_j}|^2}{D_{\omega_j}} \quad (33)$$

We determine the descritized amplitude of the vibrons $b_{\text{vib}j}$ according to

$$b_{\text{vib}j} = \sum_{\mathbf{q}, \omega_j < \omega_{\text{low}(\mathbf{k}_{\text{ex}} - \mathbf{q})} < \omega_j + \delta\omega} b_{\mathbf{q}} \quad (34)$$

The summation (34) takes only over the vibrons participating energy transfer from the upper and lower polariton modes with the wavevector \mathbf{k}_{ex} towards the discretized lower polariton mode with frequency ω_j . as

$$\Omega_{\mathbf{k}}(t) = 0, \text{ for } \mathbf{k} \neq \mathbf{k}_{\text{ex}} \quad (35)$$

The process of energy transfer from the higher-lying states to the bottom of lower polariton branch can be formally represented as a set of elementary 3-body interactions, where a vibron with a wavevector \mathbf{q} and a lower polariton with a quasimomentum $\mathbf{k}_{\text{ex}} - \mathbf{q}$ are created following annihilation of polariton with in-plane momentum $\hbar\mathbf{k}_{\text{ex}}$. Using momentum-to-energy mapping procedure above (34)-(35), we end up with the descritized version of the Eqs. (28)-(30) in frequency space.

$$\frac{ds_{\text{up}\mathbf{k}_{\text{ex}}}}{dt} = -i\omega_{\text{up}\mathbf{k}_{\text{ex}}} s_{\text{up}\mathbf{k}_{\text{ex}}} - \frac{1}{2}\gamma_{\text{up}\mathbf{k}_{\text{ex}}} s_{\text{up}\mathbf{k}_{\text{ex}}} + ig \sum_{j=0}^N \cos \varphi_{\mathbf{k}_{\text{ex}}} \frac{\sin \varphi_j s_{\text{low}\omega_j} b_{\text{vib}j}}{D_{\omega_j}} - i\Omega_{\mathbf{k}_{\text{ex}}}(t) \cos \varphi_{\mathbf{k}_{\text{ex}}} e^{-i\omega_{\Omega}t} \quad (36)$$

$$\frac{ds_{\text{low}\mathbf{k}_{\text{ex}}}}{dt} = -i\omega_{\text{low}\mathbf{k}_{\text{ex}}} s_{\text{low}\mathbf{k}_{\text{ex}}} - \frac{1}{2}\gamma_{\text{low}\mathbf{k}_{\text{ex}}} s_{\text{up}\mathbf{k}_{\text{ex}}} + ig \sum_{j=0}^N \sin \varphi_{\mathbf{k}_{\text{ex}}} \frac{\sin \varphi_j s_{\text{low}\omega_j} b_{\text{vib}j}}{D_{\omega_j}} - i\Omega_{\mathbf{k}_{\text{ex}}}(t) \sin \varphi_{\mathbf{k}_{\text{ex}}} e^{-i\omega_{\Omega}t} \quad (37)$$

$$\begin{aligned} \frac{ds_{\text{low}\omega_j}}{dt} = & -i\omega_j s_{\text{low}\omega_j} - \frac{1}{2}\gamma_{\text{low}\omega_j} s_{\text{low}\omega_j} + ig \cos \varphi_{\mathbf{k}_{\text{ex}}} \sin \varphi_j s_{\text{up}\mathbf{k}_{\text{ex}}} b_{\text{vib}j}^* + ig \sin \varphi_{\mathbf{k}_{\text{ex}}} \sin \varphi_j s_{\text{low}\mathbf{k}_{\text{ex}}} b_{\text{vib}j}^* - \\ & - iW_{\omega_j}(t) \cos \varphi_j e^{-i\omega_j t} + \frac{1}{2} \sum_{m=0}^N \left(\gamma_{\text{low}}^{\omega_j \omega_m} \frac{|s_{\text{low}\omega_m}|^2}{D_{\omega_m}} - \gamma_{\text{low}}^{\omega_m \omega_j} \left(D_{\omega_m} + \frac{|s_{\text{low}\omega_m}|^2}{D_{\omega_m}} \right) \right) s_{\text{low}\omega_j} \end{aligned} \quad (38)$$

$$\frac{db_{\text{vib}j}}{dt} = -i\omega_{\text{vib}}b_{\text{vib}j} - \frac{1}{2}\gamma_{\text{vib}}b_{\text{vib}j} + ig \cos \varphi_{\mathbf{k}_{\text{ex}}} \sin \varphi_j s_{\text{up}\mathbf{k}_{\text{ex}}} s_{\text{low}\omega_j}^* + ig \sin \varphi_{\mathbf{k}_{\text{ex}}} \sin \varphi_j s_{\text{low}\mathbf{k}_{\text{ex}}} s_{\text{low}\omega_j}^* \quad (39)$$

where the rates, frequencies and coupling parameters are reformulated accordingly: $\gamma_{\text{low}\omega_j} = \gamma_{\text{low}\mathbf{k}}$ and $\sin \varphi_{\omega_j} = \sin \varphi_{\mathbf{k}}$ with \mathbf{k} such that $\omega_{\text{low}\mathbf{k}} = \omega_j$; $\gamma_{\text{low}}^{\omega_j\omega_m} = \gamma_{\text{low}}^{\mathbf{k}\mathbf{k}'}$ with \mathbf{k} and \mathbf{k}' such that $\omega_{\text{low}\mathbf{k}} = \omega_j$ and $\omega_{\text{low}\mathbf{k}'} = \omega_m$. Here we assume the quantities $\gamma_{\text{low}\mathbf{k}}$, $\sin \varphi_{\mathbf{k}}$ and $\gamma_{\text{low}}^{\mathbf{k}\mathbf{k}'}$ are changed slightly on the discretization scale $\delta\omega$ which is a reasonable assumption unless one applies $\delta\omega \sim T$. Note the new thermalization rates $\gamma_{\text{low}}^{\omega_j\omega_m}$ meet the same Kubo-Martin-Schwinger relation

$$\gamma_{\text{low}}^{\omega_j\omega_m} = \gamma_{\text{low}}^{\omega_m\omega_j} \exp\left(\frac{\omega_m - \omega_j}{T}\right) \quad (40)$$

According to the mapping procedure, we use the following relations in the Eqs. (36)-(39)

$$\sum_{\mathbf{k}'} \sin \varphi_{\mathbf{k}'} s_{\text{low}\mathbf{k}'} b_{\mathbf{k}-\mathbf{k}'} = \sum_j \frac{\sin \varphi_j s_{\text{low}\omega_j} b_{\text{vib}j}}{D_{\omega_j}} \quad (41)$$

$$W_{\text{low}\omega_j}(t) = \sum_{\mathbf{k}', \omega_j < \omega_{\text{low}\mathbf{k}'} < \omega_j + \delta\omega} W_{\text{low}\mathbf{k}'}(t) \quad (42)$$

II. NUMERICAL SIMULATIONS

We generate the system of differential equations based on Eqs. (36)-(39) consisting of the modes in upper and lower polariton branches at \mathbf{k}_{ex} , the most intense vibron mode with energy equals to $\omega_{\text{vib}} = 0.199$ eV and the set of equidistant $N = 120$ modes in frequency space that fill the bottom of lower polariton dispersion within the momenta range of $[|k_{\text{min}}| = 0 \mu\text{m}^{-1}, |k_{\text{max}}| = 2 \mu\text{m}^{-1}]$. All the modes are shown in Fig.S1 as green dots on top of the polariton dispersion relations. Modes at the bottom of lower polariton branch are shown in the inset of Fig.S1.

To calculate polariton dispersion relations we use standard parabolic dispersion of the cavity $\omega_{\text{cav}\mathbf{k}} = \omega_{\text{cav}0} + \alpha_{\text{cav}} \cdot \mathbf{k}^2$, where the cut-off frequency at $\mathbf{k} = 0$ is equal to $\omega_{\text{cav}0} = 2.53$ eV and the curvature parameter $\alpha_{\text{cav}} = 2.2 \cdot 10^{-3}$ eV μm^2 is given from experimental data. In turn, Frenkel excitons are well-known as dispersionless particles, therefore it is reasonable assuming the constant energy of $\omega_{\text{exc}} = 2.72$ eV. Similarly, the coupling constant between exciton and cavity modes is fixed at $\Omega_{\text{Rk}} = 0.035$ eV regardless in-plane quasimomentum

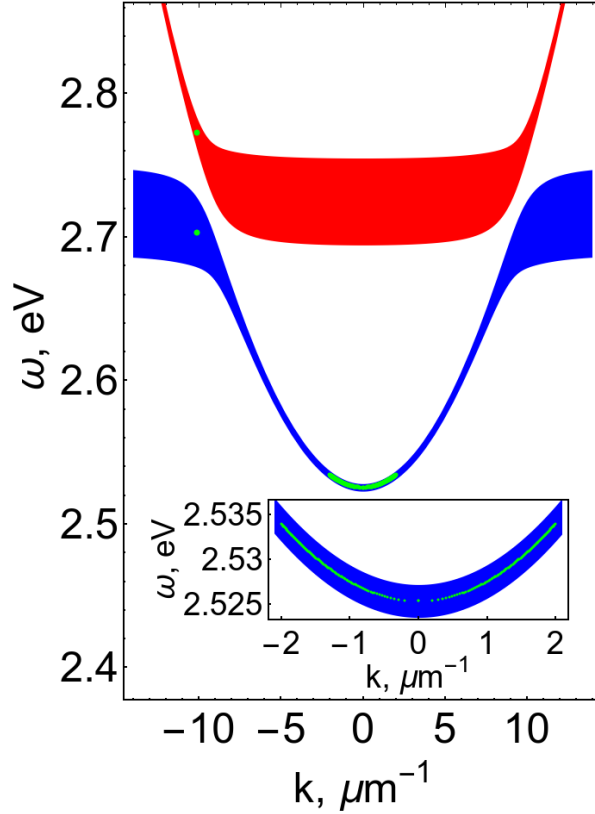


FIG. S1. The dispersion of the lower (red) and upper (blue) polariton branches. The width of the lines along the frequency axes indicates the FWHM of the polaritons, which corresponds to the dissipation rate. The discrete modes are shown as green dots.

k. The photon decay and exciton dephasing rates are assumed to be \mathbf{k} -independent values $\gamma_{\text{cav}\mathbf{k}} = 2 \cdot 10^{-3}$ eV and $\gamma_{\text{exc}} = 0.06$ eV respectively.

Finally, we use Eqs. (20),(21) to plot lower and upper polariton branches in Fig.S1, where the linewidth for both dependencies correspond to dissipation rate of the lower $\gamma_{\text{low}\mathbf{k}} = \gamma_{\text{cav}\mathbf{k}} \cos^2 \phi_{\mathbf{k}} + \gamma_{\text{exc}} \sin^2 \phi_{\mathbf{k}}$ and upper $\gamma_{\text{up}\mathbf{k}} = \gamma_{\text{cav}\mathbf{k}} \sin^2 \phi_{\mathbf{k}} + \gamma_{\text{exc}} \cos^2 \phi_{\mathbf{k}}$ polaritons respectively.

We excite our system by pump electromagnetic field which couples exciton states exactly at their resonance $\omega_{\Omega} = \omega_{\text{exc}} = 2.72\text{eV}$. The incident angle of the pump beam is $\theta = 45^\circ$ that corresponds to in-plane momentum $\hbar\mathbf{k} = 10 \mu\text{m}^{-1}$. The pump pulse duration of 150 fs corresponds to $t_{\Omega} = 2\pi \cdot 30 \text{ eV}^{-1}$. The pump frequency fulfils the resonant vibron condition $\omega_{\Omega} = \omega_{\text{low}0} + \omega_{\text{vib}}$. The vibron resonance frequency is given from experimental data $\omega_{\text{vib}\mathbf{q}} = 0.199 \text{ eV}$, while exciton-vibron interaction constant \mathbf{g} is left to be variable parameter during numerical simulations. We get the best fit results with $g = 0.45 \cdot 10^{-3} \text{ eV}$.

The value agrees well with the experimental one assessed independently using a cross-section of Raman scattering [1] and theoretical approach developed in Ref.[5].

To study dynamics of the polariton condensation and associated nonlinear emission from the organic microcavity we set thermalization rate for the lower polaritons at the level of $\gamma_{\text{low}}^{\mathbf{k}_1\mathbf{k}_2} = 0.7 \cdot 10^{-7}$ eV (it corresponds to the best fit result) for $\omega_{\text{low}\mathbf{k}_1} < \omega_{\text{low}\mathbf{k}_2}$ and use thermal energy $kT = 0.025$ eV corresponding room temperature 300K. The vibron dissipation rate is estimated from Raman spectra of MeLPPP $\gamma_{\text{vib}} = 0.0025$ eV. Following experimental conditions we choose $|k| < 0.2 \mu\text{m}^{-1}$ and $\omega_W = \omega_{\text{low}0}$ for the seed. The seed pulse duration of 200 fs corresponds to $t_\Omega = 2\pi \cdot 40 \text{ eV}^{-1}$. Finally, we apply the following initial conditions to the system: $s_{\text{up}\mathbf{k}_{\text{ex}}}(0) = 0$, $s_{\text{low}\omega_j}(0) = 0$ for all j , $b_j(0) = \sqrt{n_{\text{vib}}^{\text{th}}}$ for all j .

We simulate integrated emission as a function of dimensionless pump intensity P for the seeded (Fig.S2a, red) and spontaneously formed (Fig.S2a, black) condensates. The integration takes place within $\pm 0.2 \mu\text{m}^{-1}$ according to the experimental configurations. One can see remarkable agreement with the experimental curves represented in Fig.1b of the main text. Importantly, our model adequately describes polariton population distribution in (E, k) -space. Fig.S2b and c demonstrate spontaneously formed and seeded condensates respectively at the incident pump fluence of $P \sim 2P_{th}$. Here we use the seed pulse carrying 1000 photons which resonantly inject polaritons at the ground state. As we form macroscopic occupation of the ground state at the very beginning stage of polariton condensation, it boosts relaxation towards the ground state through the vibron-assisted bosonic stimulation. One can see the predominant population into the preoccupied states via sharp distribution of the polariton population along the lower branch. Both simulations accurately describe experimental (E, k) distributions from Fig.1b,c of the main manuscript. In fact, it manifests our microscopic theory is adequate describing physical mechanisms underlying vibron-mediated polariton condensation in the organic system at resonant excitation and seeding.

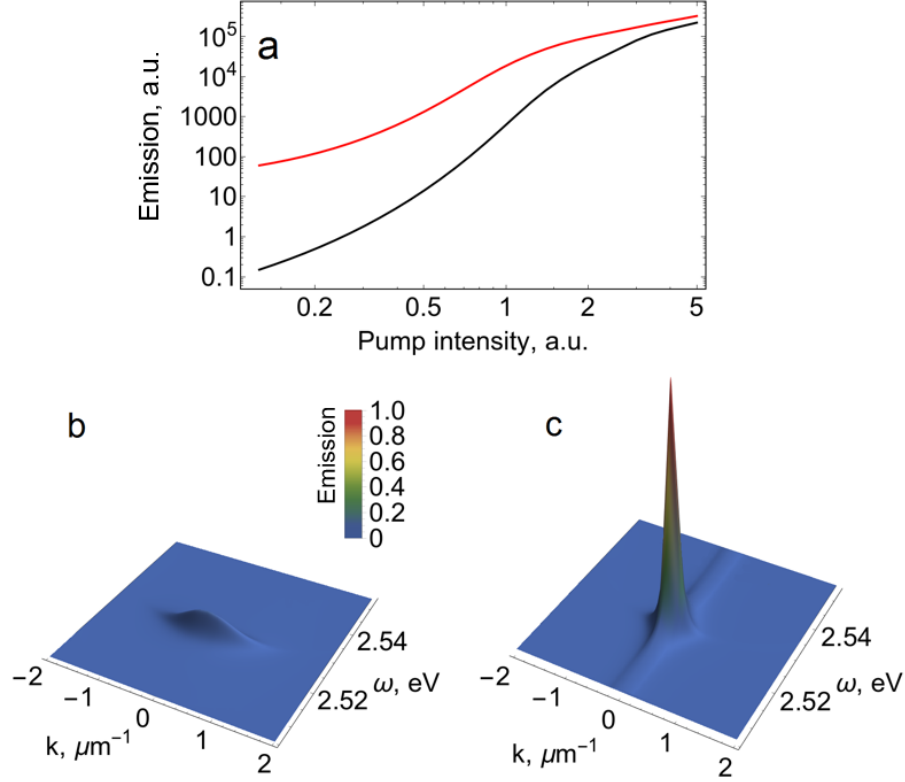


FIG. S2. a - Emission of the seeded (red) and spontaneously formed (black) condensates integrated over the polariton state within $\pm 0.2 \mu\text{m}^{-1}$ momentum range as a function of pump intensity P . b and c - Time-integrated energy, momentum (E, k) -distribution of polariton population along the lower branch for the spontaneously formed and seeded polariton condensates respectively. Population distributions are simulated at $P = 2P_{th}$

Finally, to peek behind the curtain of the extraordinary nonlinear response of the system, we examine switching contrast defined in the main manuscript as $Contrast = \frac{P_{seed}}{P_{spont}} - 1$ under different exciton-photon (Ω_R) and exciton-vibron (g) coupling constants. Figure S3 shows the contrast of switching under $\langle n \rangle = 10$ seed photons as a function of coupling constants.

With increasing exciton-photon and exciton-vibron interactions we observe further increase in contrast values followed by saturation regime. The increase of contrast is a quite intuitive result which comes from the form of master equations since both: exciton-photon and exciton-vibron coupling terms in the Hamiltonian Eq.(13),(12) favor stimulated polariton relaxation from higher energy excited states towards the ground state. Further increase of coupling constants does not gain higher switching contrast as the bosonic stimulation is already strong enough to form polariton condensate. The highly nonlinear dynamics of

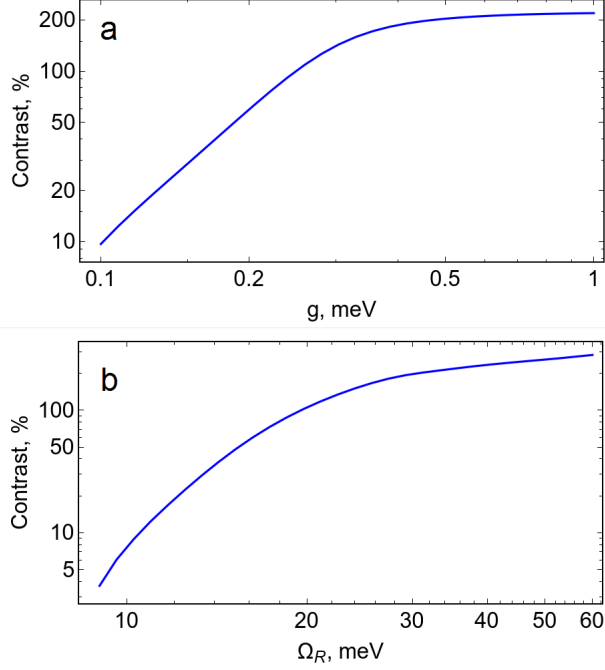


FIG. S3. **a**, The switching contrast as a function of exciton-vibron coupling (g) with the fixed exciton-photon coupling $\Omega_R = 35$ meV. **b**, The switching contrast as a function of exciton-photon coupling (Ω_R) with the fixed exciton-vibron coupling $g = 0.45$ meV. All simulations are done at the fixed pump fluence of $P = 2P_{th}$. Contrast is obtained by integration E, k distributions over the ground state momenta range of $\pm 0.2 \mu m^{-1}$

the process saturates polariton population at finite times in this regime of strong coupling terms.

III. PHOTON COUNTING OF SEED PULSES

In this section we provide with calibration data for incident photon states of the seed pulses based on direct method of counting the seed photons transmitted through the sample. The seed beam is focuses onto the sample within wavevector range of $\pm 0.2 \mu m^{-1}$. The light transmitted through the sample is coupled to a single photon avalanche Si photodiode (SAPD) idq100 (ID Quantique) equipped with a $50 \mu m$ multi-mode fiber. To get rid of the noise we implement time-gated photon counting scheme using time-correlated single photon counting module SPC-160 (Becker & Hickel GMBH). We employ a standard inverse START-STOP technique to detect the photon events within 1 ns time window allowing for

noise-free measurements. A photon detected on SAPD initiates photon counting routine while the signal from the master laser terminates the measurement. We have carried out photon counting experiments at 500Hz repetition rate applying five different seed energies that correspond to 2050, 143, 45, 12 and 3.5 photons per pulse in average, within the linewidth of the ground polariton state. Further on we have quantified integrated photon detection efficiency (η), including transmittance of the sample (T), light coupling (K) and quantum efficiency (QE) of the SAPD: $\eta = T \cdot K \cdot QE \approx 0.01$. Figure S4 shows an average photon count rate per seed pulse integrated over 60000 pulses (collection time of 120s) versus the average number of photons per pulse incident on the SAPD taking into account integrated detection efficiency η .

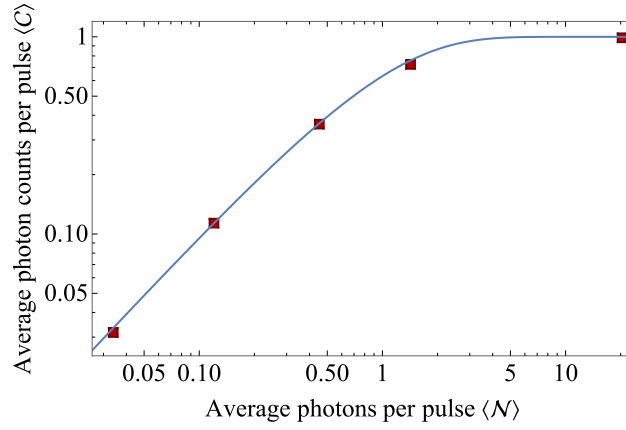


FIG. S4. The average photon counts per pulse $\langle C \rangle$ detected by the single photon counting setup within 120s collection time as the function of the average photon numbers per seed pulse $\langle N \rangle$. The blue curve shows model values of $\langle C \rangle$ expected from theory for Poisson-distributed pulses, according analytic expression $\sum_{m=1}^{\infty} \frac{\langle n \rangle^m e^{-\langle n \rangle}}{m!}$.

One can observe a clear linear dependence for the photon counts at the low incident photon numbers $\langle N \rangle \ll 1$ that saturates in the vicinity of $\langle N \rangle = 1$ with the maximum value of $\langle C \rangle$ equals 1 at $\langle N \rangle \gg 1$. The upper limit of $\langle C \rangle = 1$ relates to an operation principle of SAPD which generates a constant signal upon photon arrival regardless of the incident photon flux. The overall trend can be quantitatively explained in terms of summation over the probabilities to have at least one photon per seed pulse. Obeying Poisson distribution the sum defines exactly as $\sum_{m=1}^{\infty} \frac{\langle n \rangle^m e^{-\langle n \rangle}}{m!}$. We plot the analytic expression in Figure S4 (blue curve). It reproduces our experimental observation in a very precise way that verifies

our photon numbers calibration and serves as the independent proof of Poisson distribution of the seed beam.

-
- [1] Somitsch, D *et al.* The Raman spectra of methyl substituted ladder type poly (p-phenylene): Theoretical and experimental investigations. *Synthetic Metals* **138**, 39–42 (2003).
- [2] Born, M. & Oppenheimer, R. Quantum Chemistry: Classic Scientific Papers. *World Scientific 20th Century Chemistry* **8**, 1–24 (2000).
- [3] Carmichael, H. An open systems approach to quantum optics. *Springer-Verlag*, Berlin (1991).
- [4] Scully, M.O., Zubairy, M.S. Quantum optics. *Cambridge University Press*, Cambridge (1997).
- [5] Shishkov, V *et al.* Enhancement of the Raman Effect by Infrared Pumping. *Phys. Rev. Lett.* **122**, 153905 (2019).